Korean J. Chem. Eng., 32(12), 2406-2411 (2015)
DOI: 10.1007/s11814-015-0080-4

pISSN: 0256-1115
eISSN: 1975-7220

Kinematic analyses of a cross-slot microchannel applicable to cell deformability measurement under inertial or viscoelastic flow

Ju Min Kim[*,**,†]

*Department of Chemical Engineering, Ajou University, Suwon 443-749, Korea
**Department of Energy Systems Research, Ajou University, Suwon 443-749, Korea
(*Received 4 March 2015 • accepted 13 April 2015*)

Abstract−A cross-slot microchannel has been harnessed for a wide range of applications, such as label-free measurements of cell deformability and rheological characterization of complex fluids. This work investigates flow kinematics in a cross-slot microchannel used for the measurements of cell deformability utilizing finite element method (FEM)-based numerical simulation. In a cross-slot microchannel, the cell is stretched near the stagnation of the cross-slot channel, and cell deformation is significantly affected by its trajectory. Two passive methods, inertia- and viscoelasticity-based, which do not rely on any external force such as an electric field, have been applied to focus particles along the channel centerline so that the cell trajectories are unified. However, it is not well understood how the flow kinematics inside the cross-slot channel is altered by the inertial or viscoelastic effect when these two methods are employed. This work demonstrates that the flow kinematics such as the distributions of flow type and strain rate is notably changed with an increase in the Reynolds number when an inertia-based method is employed. On the other hand, flow kinematics does not significantly deviate from that of an inertia-less Newtonian fluid irrespective of the Weissenberg numbers when a viscoelasticity-based method is used. The current work will be helpful for the design and operation of a cross-slot microdevice for measuring cell deformability.

Keywords: Cross-slot Microchannel, Cell Deformability, Particle Focusing, Numerical Simulation

INTRODUCTION

Live cells are deformed under external fields such as an optical or hydrodynamic force [1-4]. The cell deformability represents the pathophysiological conditions of the human body or cell itself [5,6]. For instance, the deformability of red blood cells (RBCs) is significantly altered when the human body contracts malaria or diabetes [7]. Thus, cell deformability measurements have been efficient biomarkers for the diagnosis of diseases or cell health [3,8-10], which is attractive because it requires nether a complicated nor expensive labeling procedure [5]. Further, the deformability of the cells can be measured by optical microscopy in a high throughput manner, which guarantees a fast but accurate measurement of their deformability [8-10]. Microfluidics-based deformability measurements have recently attracted significant attention because the flow can be precisely controlled, and the procedures for a deformability measurement can potentially be automated [5]. The design of a microchannel shape, which generates flow fields to deform the cells, is a key technology in such microfluidics-based approaches.

As previously discussed by Cha et al. [3], the planar extensional flow field generated by a cross-slot microchannel has been used for the deformation of materials such as cells [2,3,8] and DNA [11] because its affine deformation increases exponentially as the strain experienced by a deformable particle increases [12]. Further, its flow type does not include any rotational components [13]. Thus, the deformation of the materials by an extensional flow field is larger compared to the deformation in a shear flow, which is relevant in a pressure-driven channel flow [13]. A shear flow is a weak flow in which the affine deformation of a deformable particle is linearly increased with an increase in the strain [12], and the particle deformation is significantly hindered by the rotational motion [13]. In a cross-slot microchannel, as shown in Fig. 1(a), a deformable particle such as an RBC, which emanates from the inlets (top and bottom channels), is stretched near the stagnation point (central point) and then moves toward the outlets (right and left channels). However, the deformability of a cell can be measured differently according to its spatial trajectory irrespective of its intrinsic physical properties because the flow kinematics, such as the local strain rate and flow type in a practical device, is not spatially homogeneous [3,14]. Thus, unification of the cell trajectory prior to a deformability measurement is an essential step for an accurate deformability measurement [3,5].

Particles migrate laterally toward positions of equilibrium under channel flows when a fluid flow is inertial (still laminar) [15] or viscoelastic [16]. Recently, such phenomena have been extensively exploited to manipulate particles in a microfluidic channel [17-28]. Researchers have also engineered such phenomena to focus the particles along the channel centerline to unify particle trajectories [2,3]. The two passive methods of inertial and viscoelastic particle focusing are attractive because they do not require any external force such as an electric field despite the particles being tightly focused along the channel centerline through a purely hydrodynamic effect

†To whom correspondence should be addressed.
E-mail: jumin@ajou.ac.kr

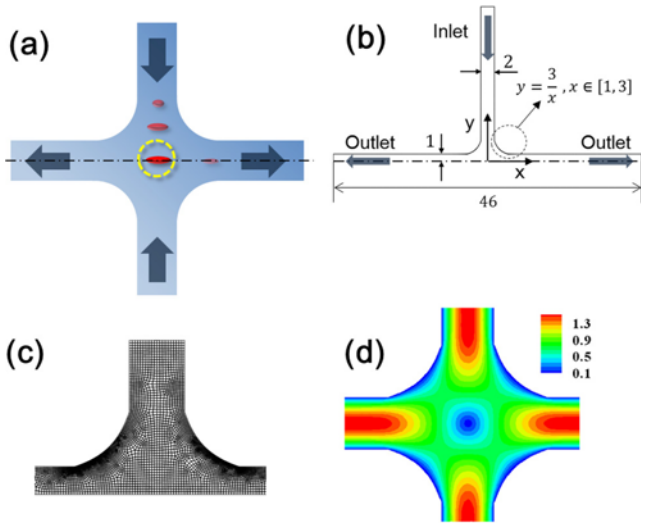

Fig. 1. (a) Schematic diagram of a cross-slot microchannel used to measure cell deformability. Cells are emanating from two inlets (top and bottom channels), and the cells approach the stagnation point (central point). The cells are highly stretched near the stagnation point and move toward the outlets (right and left channels). The cell deformability is measured by analyzing the image of a deformed cell near the stagnation point [2,3], and the same procedure is repeated for a number of cells to obtain statistically relevant data. (b) Computational domain used for the numerical simulation, which is equivalent to the geometry used by Cha et al. [3]. The inlet and outlets are far enough to be unaffected by the cross-slot region, and the distances from the inlet and the outlets to the central point are equal. The lower dash-dotted line denotes a symmetric line. (c) Magnified view of a finite element mesh near the central point. (d) Velocity magnitude distribution at Re=0 and Wi=0 (note that all of the numerical solutions in this work were obtained using the finite element mesh presented in Fig. 1(c), but mirror images were added to help with an understanding of the results shown in Figs. 1, 3, 4, and 6).

[2,3,17,18,20]. However, it is not yet well understood how the local kinematics inside a cross-slot channel is affected by the inertia and viscoelasticity, i.e., flow parameters such as the Reynolds (Re) and Weissenberg (Wi) numbers. The Reynolds number denotes the relative ratio of inertial to viscous forces, and the Weissenberg number is used to characterize the ratio of elastic to viscous properties for viscoelastic fluids [29].

Although several previous researches have already investigated the flow dynamics in a cross-slot geometry, they are mostly limited to characterizing the rheological properties of complex fluids such as the extensional properties [30,31] or the prediction of flow instabilities occurring in a cross-slot channel [32]. Otherwise, numerical studies related to a material deformation have been restricted to inertia-less Newtonian cases (Re=0) [11] or a viscoelastic flow with a specific Weissenberg number [3] as a supplement to the experimental data. In this work, the focus is on comparative studies showing how inertia or viscoelasticity affects the flow kinematics, such as the flow type and strain rate distribution in a cross-slot device, for a wide range of flow parameters of Re and Wi numbers. The flow kinematics was investigated utilizing FEM-based numerical simulations with a constitutive modeling (upper convective Maxwell (UCM) model [29]) for a viscoelastic fluid. The flow kinematics inside a cross-slot channel is shown to be significantly different according to whether an inertial or viscoelastic particle focusing method is used. The current study is expected to provide useful information and insight into the design and analysis of a microdevice for cell deformability measurements.

GOVERNING EQUATIONS AND BOUNDARY CONDITIONS

The cell deformability has been measured under the inertial Newtonian and inertia-less viscoelastic flow conditions. A poly(vinylpyrrolidone) (PVP) mixture in a buffered solution, i.e., phosphate-buffered saline (PBS), was used as a viscoelastic fluid with nearly constant shear viscosity [33], which can be modeled as a UCM model [3,19]. The cross-slot geometry considered in this work is shown in Fig. 1(b). The mathematical modeling for such a fluid flow is composed of continuity, momentum balance, and constitutive (UCM) equations. This study considers a two-dimensional steady problem, and the dimensionless forms of the governing equations can be represented as follows:

$$\nabla \cdot \mathbf{u} = 0 \tag{1}$$

$$\mathrm{Re}(\mathbf{u} \cdot \nabla \mathbf{u}) = -\nabla p + \nabla \cdot \boldsymbol{\tau} \tag{2}$$

$$\boldsymbol{\tau} + \mathrm{Wi}[\mathbf{u} \cdot \nabla \boldsymbol{\tau} - (\nabla \mathbf{u})^T \cdot \boldsymbol{\tau} - \boldsymbol{\tau} \cdot (\nabla \mathbf{u})] = [(\nabla \mathbf{u}) + (\nabla \mathbf{u})^T] \tag{3}$$

where $\mathbf{u}$ is the velocity vector, p is the pressure field, and $\boldsymbol{\tau}$ is the extra stress tensor, and all of the variables are dimensionless. In the equations, '·' denotes a dot product and $(\mathbf{a})^T$ is the transpose of tensor $(\mathbf{a})$. In addition, Re and Wi are defined by h<u>ρ/μ and λ<u>/h, respectively (note that the current definition of Wi is equivalent to twice the Deborah number (De) defined by Cha et al. [3]), h is half of the channel width, <u> is the average velocity in the channel cross section, ρ is the fluid density, and μ and λ are the shear viscosity and relaxation time of a fluid, respectively. In the equations, the length of scale was normalized using h, velocity $\mathbf{u}$ was non-dimensionalized using <u>, and p and τ were scaled using μ<u>/h. The UCM model is reduced to a Newtonian fluid case when Wi is set to zero [29].

In the computational domain shown in Fig. 1(b), a fully developed velocity was imposed on the inlet and outlets, a no-slip boundary condition was imposed on the channel wall, and a fully developed boundary condition of extra stresses was imposed on the inlet. In addition, a symmetric boundary condition was imposed along the symmetric line shown in Fig. 1(b). Note that this geometrical shape (Fig. 1(b)) and the symmetric flow conditions at both the inlets and outlets are equivalent to that used by Cha et al. [3].

NUMERICAL METHODS

The governing equations presented in the previous section were solved using a standard mixed finite element formation, and the numerical procedures applied in this work are identical to those of a previous work [34]. Thus, the numerical methods were briefly introduced to explicitly define the problems considered. The numer-

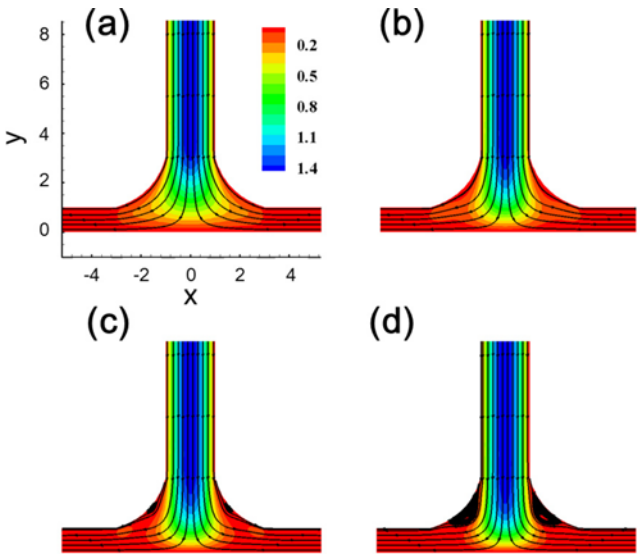

Fig. 2. Streamlines and distributions of y-component velocity field under a Newtonian flow (Wi=0): (a) Re=0, (b) Re=20, (c) Re=40, and (d) Re=160. The vortices appear when Re≥40 near the curved channels.

ical stability was enhanced using a discrete elastic viscous split stress (DEVSS)-G [35] formulation and streamline upwinding Petrov-Galerkin (SUPG) method [36], which is the standard for a numerical simulation of a viscoelastic flow [37]. The momentum balance and constitutive equations (Eqs. (2) and (3)) are transformed into the following forms using a DEVSS-G formulation, where velocity gradient tensor **G** is additionally introduced to strengthen the elliptic terms in the momentum balance equation [35].

$$\mathrm{Re}(\mathbf{u}\cdot\nabla\mathbf{u}) = -\nabla p + \nabla\cdot[(\nabla\mathbf{u}) + (\nabla\mathbf{u})^T] - \nabla\cdot(\mathbf{G}+\mathbf{G}^T) + \nabla\cdot\boldsymbol{\tau} \tag{4}$$

$$\mathbf{G} = \nabla\mathbf{u} \tag{5}$$

$$\boldsymbol{\tau} + \mathrm{Wi}[\mathbf{u}\cdot\nabla\boldsymbol{\tau} - \mathbf{G}^T\cdot\boldsymbol{\tau} - \boldsymbol{\tau}\cdot\mathbf{G}] = [\mathbf{G}+\mathbf{G}^T] \tag{6}$$

Thus, Eqs. (1), (4), (5), and (6) are governing equations in the DEVSS-G formulation. The velocity, pressure, extra stress, and velocity gradient tensor are interpolated using the Lagrangian basis function in a mixed finite element formulation as follows:

$$\mathbf{u} = \Sigma_i \psi_i \mathbf{u}_i,\ P = \Sigma_i \varphi_i p_i,\ \boldsymbol{\tau} = \Sigma_i \varphi_i \boldsymbol{\tau}_i,\ \mathbf{G} = \Sigma_i \varphi_i \mathbf{G}_i, \tag{7}$$

where ψ_i and φ_i are biquadratic and bilinear shape functions, respectively. The weak forms of Eqs. (1), (4), (5), and (6) can be represented as follows:

$$\langle \nabla\cdot\mathbf{u};\ \varphi\rangle = 0 \tag{8}$$

$$\langle \mathrm{Re}(\mathbf{u}\cdot\nabla\mathbf{u});\ \psi\rangle + \langle -p\mathbf{I} + [(\nabla\mathbf{u}) + (\nabla\mathbf{u})^T] - (\mathbf{G}+\mathbf{G}^T) + \boldsymbol{\tau};\ \nabla\psi\rangle = \langle\langle (-p\mathbf{I} + [(\nabla\mathbf{u}) + (\nabla\mathbf{u})^T] - (\mathbf{G}+\mathbf{G}^T) + \boldsymbol{\tau})\cdot\mathbf{n};\ \psi\rangle\rangle \tag{9}$$

$$\langle (\boldsymbol{\tau} + \mathrm{Wi}[\mathbf{u}\cdot\nabla\boldsymbol{\tau} - \mathbf{G}^T\cdot\boldsymbol{\tau} - \boldsymbol{\tau}\cdot\mathbf{G}] - [\mathbf{G}+\mathbf{G}^T]);\ \varphi\rangle = \mathbf{0} \tag{10}$$

$$\langle \mathbf{G} - \nabla\mathbf{u};\ \varphi\rangle = \mathbf{0} \tag{11}$$

where '< >' and '<< >>' indicate the domain and boundary integrals, respectively, **n** denotes an outward normal vector at the boundary, and **I** is the identity tensor. The modified SUPG method developed by Fan and Crochet [38] was applied to a constitutive equation, which is implemented by consistently applying the following modified weight function φ_s to Eq. (10) instead of the original weight function φ.

$$\varphi_s = \varphi + \bar{k}\hat{\mathbf{u}}_e\cdot\nabla\varphi \tag{12}$$

where $\bar{k}$ is a characteristic element length scale, and $\hat{\mathbf{u}}_e$ is the normalized velocity in an element; more detailed definitions for $\bar{k}$ and $\hat{\mathbf{u}}_e$ were presented in a previous work [34]. The solutions of the current numerical formulations based on DEVSS-G/SUPG were obtained using a Newton-Raphson/iterative solution method developed by Kim et al. [34]. L1 norm $<10^{-4}$ between two successive steps was the convergence criterion in the Newton-Raphson method. The computational domain was discretized in the finite element mesh with rectangular shape as presented in Fig. 1(c). The mesh is composed of 11,672 elements, and the number of total unknowns is 196,098. A finer mesh was also tested, but no significant differences between the two meshes were shown.

RESULTS AND DISCUSSION

As shown in Fig. 1(a), the cells emanate from the inlets and move toward the stagnation point in the cross-slot channel for a deformation measurement. The velocity of a deformable cell decreases while the cell approaches the stagnation point, as shown in Fig. 1(d), and consequently, the cell undergoes compression. Meanwhile, its velocity accelerates when the cell escapes from the stagnation point to an outlet, and thus the cell is stretched along the outlet direction (the x-axis in the current coordinate systems). On the other hand, the velocity field near the stagnation point can be represented as a saddle-like "semistable potential well" [39]. The stagnation point works as a stable potential well while a cell is approaching the stagnation point (or when the cell is compressed), but the stagnation point is no longer stable once the cell reaches it and is at its maximum in a potential landscape along the direction of the outlets (or x-axis) [39]. Therefore, it is expected that the cell eventually escapes from the stagnation point after staying at the point for a finite amount of time [39]. Meanwhile, the cells are randomly distributed in the lateral direction at the inlets. The random lateral distribution of the cells continues under an inertia-less Newtonian flow until the cells approach the stagnation point. There is a very low probability of finding randomly distributed cells passing through the stagnation point, which significantly deteriorates the efficiency of the device when measuring the deformability [3]. As previously discussed by Cha et al. [3], there is one promising way to overcome this problem, i.e., aligning the cells along the channel centerline [2,3]. In addition, the cell alignment along the channel centerline unifies the kinematic history that a cell experiences, which is helpful in avoiding different measurements of the cell deformability according to the cell trajectories [3]. In literature, inertial or viscoelastic particle focusing has been utilized to unify the trajectories of the cells [2,3].

Although microfluidic flows are usually inertia-less (or Re<<1), it has been recently demonstrated that an inertial flow can be generated even under microfluidic flow conditions. Under an inertial flow (still laminar), particles are focused along the equilibrium posi-

tions under inertial microfluidic flows, i.e., Re ~ $O(10^1)$, which has been engineered to manipulate the particles so as to count or sort the cells [17]. The number of equilibrium positions can be reduced to a single stream by modulating the width-to-height aspect ratio of the channel and combining it with a Dean flow that occurs in a curved channel [17,24]. On the other hand, inertial particle focusing has been successfully applied to unify the cell trajectories, which was accomplished by exploiting a serpentine channel before a cross-slot channel [2,8]. However, it is not well understood how the inertial flow changes the flow kinematics inside a cross-slot channel.

First, I investigated the changes in the velocity fields and the streamlines in the cross-slot channel when Re increases, as shown in Fig. 2. The y-component velocity is decelerated as a cell starting from the inlet (y>>0) approaches the stagnation point (y→0), but its deceleration is significantly delayed with an increase in Re. Consequently, it is expected that cell stretching (or compression) occurs in the inertial flows nearer the stagnation point as compared to an inertia-less Newtonian case. On the other hand, it was observed that the streamlines are dramatically changed with an increase in Re, as shown in Fig. 2, and vortices are generated near the curved walls when Re≥40, whereas no vortex formation is predicted at lower Re numbers. It is anticipated that cells will be occasionally trapped in the vortices, but these trapped cells may occasionally escape from the vortices owing to a random fluctuation of the flow field. Such cell trapping and escaping may destabilize the flow field, which can deteriorate the performance of the deformability measurement device. For a more quantitative analysis, the distribution of the flow type (Δ) defined by $\Delta=(|\mathbf{d}|-|\boldsymbol{\omega}|)/(|\mathbf{d}|+|\boldsymbol{\omega}|)$ was investigated, where $|\mathbf{d}|$ and $|\boldsymbol{\omega}|$ correspond to the magnitudes of the deformation rate tensor, $\mathbf{d}\equiv 1/2(\nabla\mathbf{u}+(\nabla\mathbf{u})^T)$, and the vorticity tensor $\boldsymbol{\omega}\equiv 1/2(\nabla\mathbf{u}-(\nabla\mathbf{u})^T)$, respectively [3,40]. The flow is purely rotational when Δ→−1, whereas it is purely extensional as Δ→1. The flow type is a shear flow when Δ=0 [40]. In a rotational flow, the cell simply rotates without stretching, whereas the cells are highly stretched in a purely extensional flow. The change in the flow type significantly affects the cell deformability measurement. Therefore, it is essential to place the cells in a purely extensional field before a deformability measurement is conducted [3]. As shown in Fig. 3, the area corresponding to Δ≈1 significantly shrinks as Re increases. Thus, both the formation of vortices and the shrinkage of a purely extensional flow region under an inertial flow require that the location of the cell deformability measurement be more strictly selected near the stagnation point with an increase in Re, as compared to an inertia-less Newtonian case. In addition, the strain rate distribution also significantly changes with an increase in Re, as shown in Fig. 4, where the strain rate is defined as the magnitude of the deformation rate tensor ($\equiv\sqrt{(1/2)\mathbf{d}:\mathbf{d}}$). In the figures, the maximum strain rate is observed at the intersections between the curved and straight channels owing to an abrupt geometrical change, but the

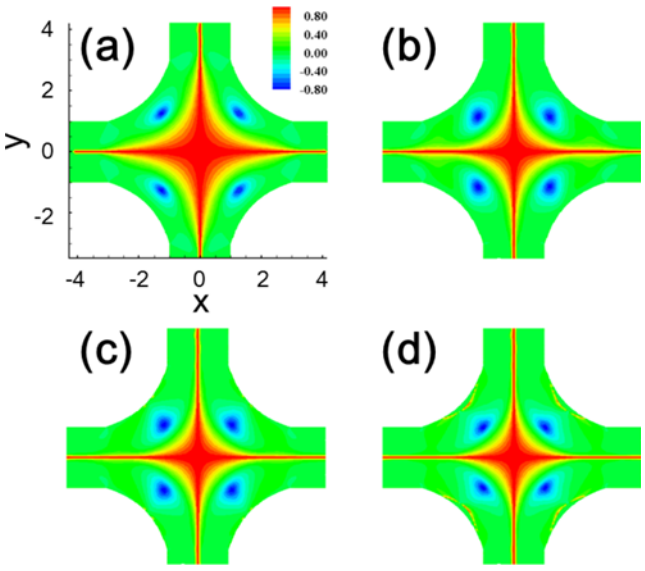

Fig. 3. Flow type (Δ) distributions under a Newtonian flow (Wi=0): (a) Re=0, (b) Re=20, (c) Re=40, and (d) Re=160. Here, Δ is defined as $\Delta=(|\mathbf{d}|-|\boldsymbol{\omega}|)/(|\mathbf{d}|+|\boldsymbol{\omega}|)$, where $|\mathbf{d}|$ and $|\boldsymbol{\omega}|$ correspond to the magnitudes of the deformation rate tensor, $\mathbf{d}\equiv 1/2\,(\nabla\mathbf{u}+(\nabla\mathbf{u})^T)$, and the vorticity tensor $\boldsymbol{\omega}\equiv 1/2(\nabla\mathbf{u}-(\nabla\mathbf{u})^T)$, respectively.

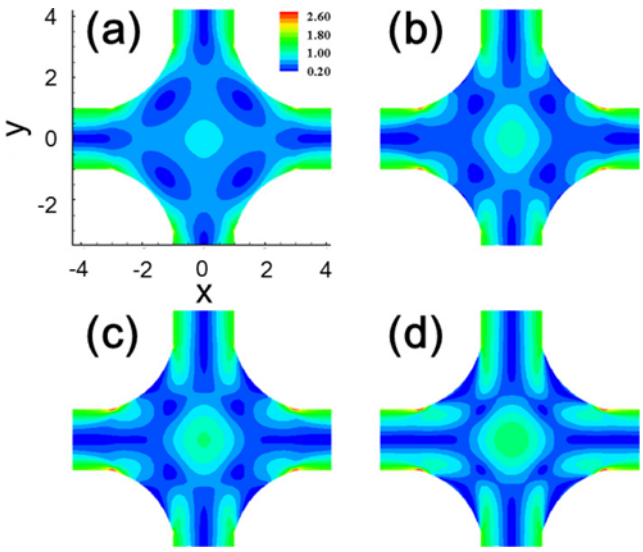

Fig. 4. Strain rate distributions under a Newtonian flow (Wi=0): (a) Re=0, (b) Re=20, (c) Re=40, and (d) Re=160. The strain rate corresponds to the magnitude of the deformation rate tensor, $\sqrt{(1/2)\mathbf{d}:\mathbf{d}}$.

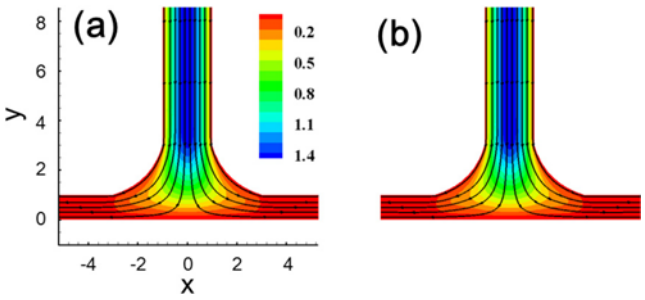

Fig. 5. Streamlines and distribution of y-component velocity field under inertia-less viscoelastic flow (Re=0): (a) Wi=0.03 and (b) Wi=0.35. No vortex development was detected, and the flow fields are almost identical to the inertia-less Newtonian case shown in Fig. 2(a).

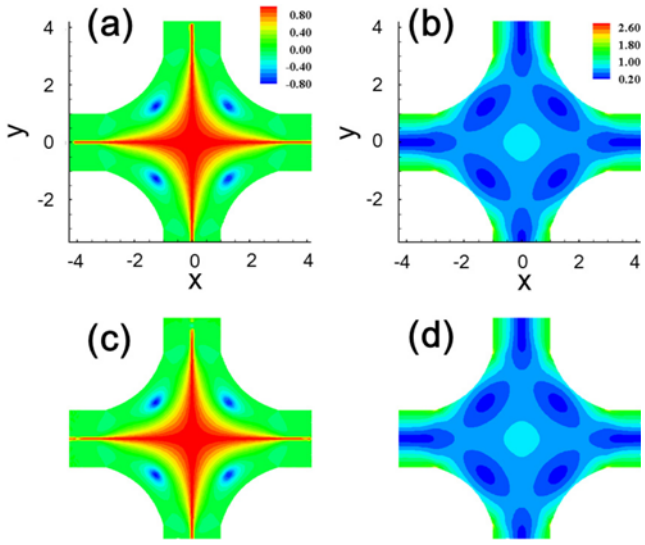

Fig. 6. Flow type (Δ) and strain rate (|d|) distributions under inertia-less viscoelastic flow (Re=0): (a) flow type, Wi=0.03; (b) strain rate, Wi=0.03; (c) flow type, Wi=0.35; and (d) flow type, Wi=0.35.

strain rate distribution near the stagnation point is relevant for the cell deformation experiments. The strain rate distribution near the stagnation point significantly deviates from that of the inertia-less Newtonian case, as shown in Fig. 4(a), and the gradient of the strain rate gradually increases with an increase in Re, which will be explained in more detail in the following paragraph. Overall, the flow kinematics under an inertial flow significantly deviates from that of an inertia-less Newtonian case as Re increases.

Meanwhile, the flow kinematics under a viscoelastic flow was almost identical to the inertia-less Newtonian case for the range of Wi numbers used in the experiments [3]. The maximum Wi number in the experiments [3] was 0.34 in terms of the current definition. As shown in Fig. 5, the flow velocity field and streamlines at both Wi=0.03 and 0.35 are almost identical to those of the inertia-less Newtonian case, i.e., Re=0 and Wi=0, as shown in Fig. 2(a). As shown in Fig. 6, the flow type and strain rate distributions under a viscoelastic flow were also investigated. The distributions deviate slightly from those of the inertia-less Newtonian cases shown in Fig. 3(a) and 4(a). The current analyses demonstrate that the flow fields inside the cross-slot channel are not significantly affected by the viscoelasticity, which is consistent with the previous result for Wi=0.2 [3]. However, these analysis results do not necessarily confirm that the flow fields inside a cross-slot channel are not insensitive to the viscoelasticity. Although a flow analysis at higher Wi numbers is necessary to address this issue, the maximum Wi is limited by the numerical convergence used in this work. Nevertheless, the current results demonstrate that the flow kinematics considered in previous experimental works [3] is almost unaffected by the viscoelasticity (at least for the range of Wi numbers considered). Finally, I compared the strain rate distributions between the inertial and viscoelastic flows inside a cross-slot geometry. As shown in Fig. 7(a), the increase in the strain rate is significantly retarded with an increasing Re as compared to the inertia-less Newtonian flow case,

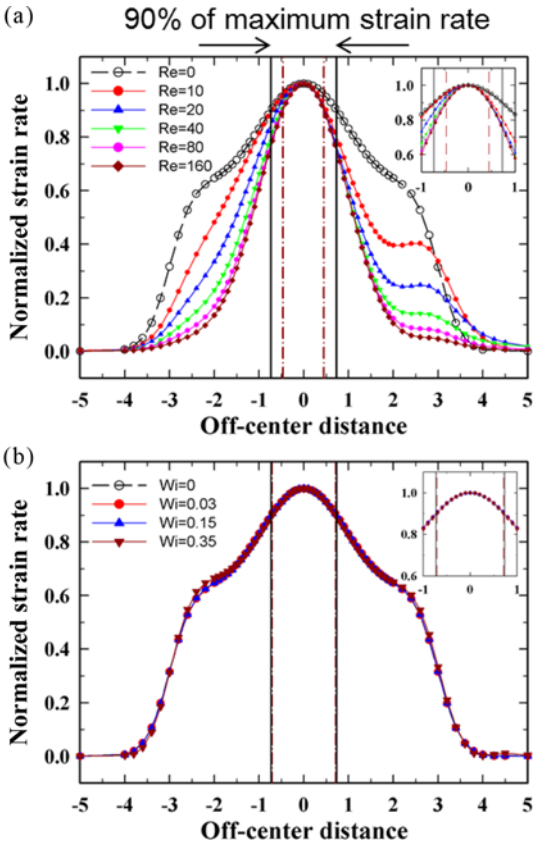

Fig. 7. Comparison of strain rate distribution between (a) inertial Newtonian and (b) inertia-less viscoelastic flow cases along the channel centerline. Here, the strain rate distribution at Re=0 and Wi=0 was inserted into both (a) and (b) for a comparison. In addition, the '–' and '+' signs of the x-axis denote the distance in the inlet and outlet directions shown in Figs. 1(a) and 1(b), respectively. Thus, these graphs demonstrate the kinematic histories when a cell moves from an inlet to an outlet along the channel centerline. In the figures, the vertical lines denote 90% of the maximum strain rate, and the insets are magnified views of the graphs near the stagnation point. The strain rate was normalized with its maximum value at the central point (stagnation point).

i.e., Re=0, and more abruptly decreases after the stagnation point, x=0. In the figure, the '–' and '+' signs of the x-axis denote the distance in the inlet and outlet directions shown in Figs. 1(a) and 1(b), respectively, following the notations by Cha et al. [3]. Interestingly, shoulders are observed for the intermediate Re numbers when the strain rate decreases, whereas the strain rate monotonically increases before the strain rate reaches its maximum. As shown in Fig. 7(a), the maximum strain rate develops at the stagnation point. However, the cell deformation was measured in the experiments when a cell enters within a criterion defined as a slightly less value than the maximum strain rate [3]. This work considers 90% of the maximum strain rate as the applied criterion. In Fig. 7(a), the strain rate around the stagnation point is shown to be rather uniform at Re=0, and the regions within the 90% criterion are denoted as vertical lines. As shown in Fig. 7(a), the regions significantly shrink with an increase in Re as compared to the inertia-less Newtonian case.

However, the regions under viscoelastic flows do not significantly change when Wi increases, as shown in Fig. 7(b).

Taken together, the flow kinematics in the inertial flows changes significantly as Re changes, but it is rather insensitive to the viscoelasticity (Wi number). Therefore, it is expected that the measurement region for the inertial particle focusing should be more tightly selected near the stagnation point as compared to the case of viscoelastic particle focusing. The current analysis results are expected to aid in the design of a deformability measurement device.

CONCLUSIONS

The effects of inertia and viscoelasticity on the flow kinematics in a cross-slot microchannel FEM-based numerical simulation have been investigated. The current analysis results demonstrate that the flow kinematics inside a cross-lot channel significantly changes with an increase in Re, but is quite insensitive to the viscoelasticity for the range of experimental conditions considered. However, the results of the current analyses do not necessarily demonstrate that a deformability measurement device based on viscoelastic particle focusing is superior to an inertial particle focusing based device. For practical applications, throughput, easy manipulation of the device, and wide operation window, including the current analysis results, should be considered simultaneously in the selection of the cell focusing method. Nevertheless, the current analysis will be helpful for guiding the selection of the location for a cell deformability measurement according to the flow conditions such as the Reynolds and Weissenberg numbers.

ACKNOWLEDGEMENTS

This research was supported by the research program of the National Research Foundation of Korea (NRF) funded by the Ministry of Education, Science, and Technology (No. NRF-2013R1A1A1A05007406).

REFERENCES

1. J. Guck, R. Ananthakrishnan, H. Mahmood, T. J. Moon, C. C. Cunningham and J. Kas, *Biophys. J.*, **81**, 767 (2001).
2. D. R. Gossett, H. T. Tse, S. A. Lee, Y. Ying, A. G. Lindgren, O. O. Yang, J. Rao, A. T. Clark and D. Di Carlo, *Proc. Natl. Acad. Sci. U.S.A.*, **109**, 7630 (2012).
3. S. Cha, T. Shin, S. S. Lee, W. Shim, G. Lee, S. J. Lee, Y. Kim and J. M. Kim, *Anal. Chem.*, **84**, 10471 (2012).
4. S. S. Lee, Y. Yim, K. H. Ahn and S. J. Lee, *Biomed. Microdevices*, **11**, 1021 (2009).
5. D. Di Carlo, *J. Lab. Autom.*, **17**, 32 (2012).
6. S. Suresh, J. Spatz, J. P. Mills, A. Micoulet, M. Dao, C. T. Lim, M. Beil and T. Seufferlein, *Acta Biomater.*, **1**, 15 (2005).
7. S. Chien, *Annu. Rev. Physiol.*, **49**, 177 (1987).
8. H. T. K. Tse, D. R. Gossett, Y. S. Moon, M. Masaeli, M. Sohsman, Y. Ying, K. Mislick, R. P. Adams, J. Rao and D. Di Carlo, *Sci. Transl. Med.*, **5**, 212ra163 (2013).
9. D. R. Gossett, H. T. K. Tse, S. A. Lee, Y. Ying, A. G. Lindgren, O. O. Yang, J. Rao, A. T. Clark and D. Di Carlo, *Proc. Natl. Acad. Sci. U.S.A.*, **109**, 7630 (2012).
10. O. Otto, P. Rosendahl, A. Mietke, S. Golfier, C. Herold, D. Klaue, S. Girardo, S. Pagliara, A. Ekpenyong, A. Jacobi, M. Wobus, N. Topfner, U. F. Keyser, J. Mansfeld, E. Fischer-Friedrich and J. Guck, *Nat. Meth.*, **12**, 199 (2015).
11. R. Dylla-Spears, J. E. Townsend, L. Jen-Jacobson, L. L. Sohn and S. J. Muller, *Lab Chip*, **10**, 1543 (2010).
12. R. I. Tanner and R. R. Huilgol, *Rheol. Acta*, **14**, 959 (1975).
13. D. E. Smith, H. P. Babcock and S. Chu, *Science*, **283**, 1724 (1999).
14. J. M. Kim and P. S. Doyle, *Lab Chip*, **7**, 213 (2007).
15. G. Segré and A. Silberberg, *Nature*, **189**, 209 (1961).
16. A. Karnis, S. G. Mason and H. L. Goldsmith, *Nature*, **200**, 159 (1963).
17. D. Di Carlo, D. Irimia, R. G. Tompkins and M. Toner, *Proc. Natl. Acad. Sci. U.S.A.*, **104**, 18892 (2007).
18. A. M. Leshansky, A. Bransky, N. Korin and U. Dinnar, *Phys. Rev. Lett.*, **98**, 234501 (2007).
19. S. Yang, S. S. Lee, S. W. Ahn, K. Kang, W. Shim, G. Lee, K. Hyun and J. M. Kim, *Soft Matter*, **8**, 5011 (2012).
20. S. Yang, J. Y. Kim, S. J. Lee, S. S. Lee and J. M. Kim, *Lab Chip*, **11**, 266 (2011).
21. J. Y. Kim, S. Ahn, S. S. Lee and J. M. Kim, *Lab Chip*, **12**, 2807 (2012).
22. A. Karimi, S. Yazdi and A. M. Ardekani, *Biomicrofluidics*, **7**, 021501 (2013).
23. X. C. Xuan, J. J. Zhu and C. Church, *Microfluid. Nanofluid.*, **9**, 1 (2010).
24. D. Di Carlo, *Lab Chip*, **9**, 3038 (2009).
25. H. Amini, W. Lee and D. Di Carlo, *Lab Chip*, **14**, 2739 (2014).
26. G. Romeo, G. D'Avino, F. Greco, P. A. Netti and P. L. Maffettone, *Lab Chip*, **13**, 2802 (2013).
27. G. D'Avino, G. Romeo, M. M. Villone, F. Greco, P. A. Netti and P. L. Maffettone, *Lab Chip*, **12**, 1638 (2012).
28. K. Kang, S. S. Lee, K. Hyun, S. J. Lee and J. M. Kim, *Nat. Commun.*, **4**, 2567 (2013).
29. R. B. Bird, Armstrong, R. C. and Hassager, O., Dynamics of Polymeric Liquids, Wiley Interscience, New York (1987).
30. B. Puangkird, F. Belblidia and M. F. Webster, *J. Non-Newt. Fluid Mech.*, **162**, 1 (2009).
31. S. J. Haward, M. S. N. Oliveira, M. A. Alves and G. H. McKinley, *Phys. Rev. Lett.*, **109**, 128301 (2012).
32. R. J. Poole, M. A. Alves and P. J. Oliveira, *Phys. Rev. Lett.*, **99**, 164503 (2007).
33. S. Cha, K. Kang, J. You, S. Im, Y. Kim and J. Kim, *Rheol. Acta*, **53**, 927 (2014).
34. J. M. Kim, C. Kim, K. H. Ahn and S. J. Lee, *J. Non-Newt. Fluid Mech.*, **123**, 161 (2004).
35. A. W. Liu, D. E. Bornside, R. C. Armstrong and R. A. Brown, *J. Non-Newt. Fluid Mech.*, **77**, 153 (1998).
36. A. N. Brooks and T. J. R. Hughes, *Comput. Method. Appl. M.*, **32**, 199 (1982).
37. R. G. Owens and T. N. Phillips, Computational Rheology, World Scientific Publishing Co., Singapore (2002).
38. Y. Fan and M. J. Crochet, *J. Non-Newt. Fluid Mech.*, **57**, 283 (1995).
39. M. Tanyeri, E. M. Johnson-Chavarria and C. M. Schroeder, *Appl. Phys. Lett.*, **96**, 224101 (2010).
40. J. S. Lee, R. Dylla-Spears, N. P. Teclemariam and S. J. Muller, *Appl. Phys. Lett.*, **90**, 074103 (2007).